Nano Research

Open Access

Research Article

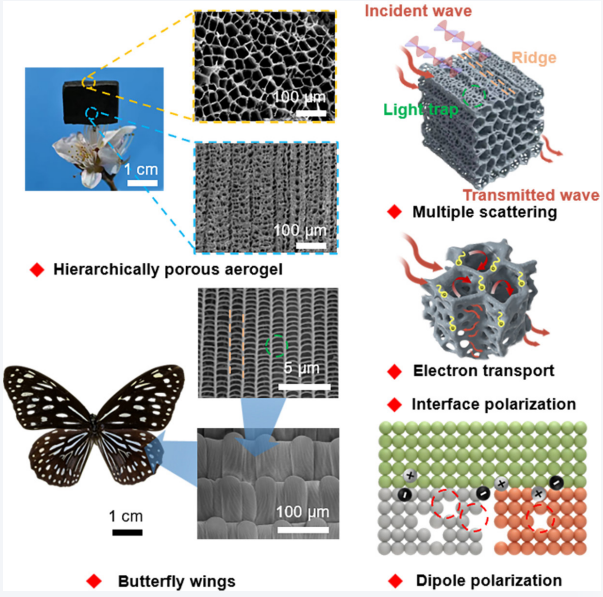
Hierarchically porous aerogels with heterogeneous nanodomains constructed from sub-1 nm nanowires for efficient microwave absorption

Tao Zhang[1], Baoqiang Bai[1], Gaofeng Shao[2] ✉, Yuxiang Du[1], Rui Fu[1], and Huazheng Sai[1] ✉

[1] *School of Chemistry and Chemical Engineering, Inner Mongolia University of Science & Technology, Baotou 014010, China*
[2] *School of Chemistry and Materials Science, Jiangsu Key Laboratory of New Energy Devices and Interface Science, Nanjing University of Information Science & Technology, Nanjing 210044, China*

Cite this article: *Nano Research*, **2027**, *20*, 94908689. https://doi.org/10.26599/NR.2026.94908689

ABSTRACT: Engineering hierarchically porous and heterogeneous interfaces is a powerful strategy for obtaining high-performance microwave absorbers, because it simultaneously improves impedance matching and enhances polarization loss. However, the coordinated construction of both macro/micro pore structures and a heterogeneous skeleton in a single-material system remains a significant challenge. Inspired by the intricate architecture of butterfly wings, the aerogels featuring aligned micro-channels and periodic nanoscale ridges were constructed from gadolinium (Gd) and bismuth (Bi)-based sub-1 nm nanowires via freeze casting. The coexistence of cellular pores and porous cell walls optimizes the impedance matching and promotes multiple scattering, while the internal nanodomain, comprising an amorphous phase alongside crystalline Gd_2MoO_6 and Bi, creates synergistic Schottky and amorphous/crystalline heterointerfaces. These interfaces enable substantial charge transfer and redistribution, thereby generating interfacial dipoles and intensifying Maxwell–Wagner polarization. Consequently, the optimized aerogel exhibits a maximum effective absorption bandwidth of 8.3 GHz and a minimum reflection loss of −57.6 dB. This work pioneers the use of sub-1 nm nanowires as building blocks for the *in situ* construction of hierarchically porous aerogels with heterogeneous nanodomains, paving the way for advanced microwave absorption materials.



KEYWORDS: hierarchically porous aerogels, heterogeneous nanodomains, sub-1 nm nanowires, microwave absorption

1 Introduction

The escalating advancements in wireless communication and electronic devices have intensified electromagnetic pollution, driving an urgent demand for high-performance microwave absorption materials (MAMs) [1, 2]. The core challenge in designing high-performance MAMs is the simultaneous achievement of excellent impedance matching and a strong attenuation capability [3–5]. Early research primarily focused on conventional materials such as carbon-based structures and ferrites [6]. Although carbon materials such as graphene and carbon nanotubes offer strong dielectric loss, their high conductivity often leads to poor impedance matching and surface reflection [7–9]. Furthermore, although ferrites provide magnetic loss, their low Snoek's limit restricts their application at high frequencies [10–12].

Researchers have developed more sophisticated strategies to overcome these limitations. Recent studies have demonstrated the construction of hierarchically porous structures is an effective strategy to optimize impedance matching. For example, carbon-

Received: March 26, 2026
Accepted: March 30, 2026

✉Address correspondence to Huazheng Sai, shz15@tsinghua.org.cn; Gaofeng Shao, gfshao@nuist.edu.cn

based aerogels have been extensively explored for their three-dimensional porous networks, which not only reduce the effective density but also entrap incident waves through multi-scattering [13]. In parallel, the engineering of heterogeneous interfaces has been identified as a powerful method to enhance polarization loss [14–16]. Seminal works on metal–organic frameworks-derived composites and magnetic-carbon hybrids have shown that interfaces between different components can induce significant interfacial polarization, known as the Maxwell–Wagner–Sillars effect [17–19]. Therefore, the integration of hierarchical porosity and heterogeneous interfaces is widely recognized as a synergistic route to high-performance MAMs [20–22]. However, most existing methods achieve these two features through separate, often complex, multi-step processes. For example, a porous scaffold might first be constructed and then secondarily loaded with heterogeneous nanoparticles, which can lead to issues like inhomogeneous distribution, poor interfacial bonding, and structural instability. The coordinated, *in-situ* construction of a monolithic material possessing both well-defined macro/micro pores and an intrinsically heterogeneous skeleton remains a significant and largely unmet challenge.

Inspired by nature's ingenious designs, which often offer elegant solutions to complex engineering problems, we focused on the butterfly wings. Their intricate architecture, featuring aligned micro-channels and periodic nanoscale ridges, is a natural masterpiece for manipulating electromagnetic waves (EMWs) and provides an ideal blueprint for microwave absorption [23–25]. To replicate this sophisticated structure, sub-1 nm nanowires (SNWs) were selected as fundamental building blocks [26–28]. Compared with conventional nanowires, sub-1 nm nanowires possess a nearly 100% surface atomic ratio and exhibit pronounced surface effects and quantum confinement effects, which induce built-in electric fields (BIEFs). BIEFs facilitate directional charge migration and interfacial polarization, significantly boosting polarization loss and impedance matching to enhance absorption efficiency [29].

In this study, Gd and Bi-based SNWs were assembled into monolithic Gd-SNWs and GdBi-SNWs aerogels using a freeze-casting technique [30]. After high-temperature pyrolysis, the aerogels exhibited interconnected cellular pores and porous cell walls. As a result, the optimized aerogel exhibits enhanced microwave absorption performance, with a maximum effective absorption bandwidth (EAB_{max}) of 8.3 GHz at a thickness of 2.8 mm and a minimum reflection loss (RL_{min}) of −57.6 dB. This work bridges bio-inspiration and advanced nanomaterial assembly, revealing the immense potential of SNWs for building complex architectures for efficient microwave absorption.

2 Experimental section

2.1 Materials

Oleic acid ($C_{18}H_{34}O_2$, OA), oleylamine ($C_{18}H_{37}N$, OM), 1-octadecene ($C_{18}H_{36}$), gadolinium chloride hexahydrate ($GdCl_3{\cdot}6H_2O$), phosphomolybdic acid hydrate ($H_3[P(Mo_3O_{10})_4]{\cdot}xH_2O$), and bismuth nitrate pentahydrate ($Bi(NO_3)_3{\cdot}5H_2O$) were obtained from Macklin. Ethanol absolute (C_2H_5OH) and cyclohexane (C_6H_{12}) were obtained from Tianjin Bohua Chemical Reagents.

2.2 Synthesis of Gd-SNWs and Bi-SNWs

Gd-SNWs were synthesized through a hydrothermal synthesis method. 0.8 g $GdCl_3{\cdot}6H_2O$ was dispersed in 12 mL C_2H_5OH and 1 mL deionized water, and then added into the mixed dispersion of 4 mL OM and 2 mL OA with stirring. Next, the reactants were placed in a 50 mL reactor using 170 °C heating for 4 h. After the reaction, the viscous dispersion was dispersed with cyclohexane and precipitated by centrifugation with C_2H_5OH. The supernatant was then poured off and the precipitate was again dispersed using cyclohexane and centrifuged using C_2H_5OH to purify the Gd-SNWs.

0.8 g $H_3[P(Mo_3O_{10})_4]{\cdot}xH_2O$ and 0.20 g $Bi(NO_3)_3{\cdot}5H_2O$ were dispersed in 16 mL deionized water. 10 mL 1-octadecene and 6 mL OM were added under vigorous stirring. Next, the reaction was sealed in a reaction kettle heated using 180 °C for 8 h. Eventually the product was collected by washing three times with cyclohexane and ethanol. The above SNWs were prepared according to the method previously reported by Wang and co-workers [31, 32].

2.3 Preparation of Gd-SNWs and GdBi-SNWs aerogels

The purified SNWs dispersed by using cyclohexane were washed by ethanol and centrifugated two times at 10,000 rpm for 10 min. Then the supernatant was poured away and solids were left behind. By weighing solids of different masses and dispersing them in cyclohexane, cyclohexane dispersion with the concentration of 6% was prepared. The cyclohexane dispersions were poured into molds for freeze casting, followed by freeze drying 24 h to obtain Gd-SNWs aerogel.

The purified Bi-SNWs and Gd-SNWs dispersed by using cyclohexane were washed by ethanol and centrifugated two times at 10,000 rpm for 10 min. Then the supernatant was poured away, and solids were left behind. Based on a quality concentration of 6%, we weighed out Gd-SNWs and Bi-SNWs in mass ratios of 2:1 and 1:1, respectively. Subsequently, the weighed Gd-SNWs and Bi-SNWs were mixed into cyclohexane solvent to form a homogeneous dispersion system by thorough stirring. The mixed solution was processed by freeze-casting to form a specific oriented structure, and then vacuum dried to remove the solvent, and finally the composite sub-1 nm nanowire aerogel material with controllable composition was successfully prepared, which was noted as GdBi*x*, where *x* represents the mass ratio of Gd-SNWs and Bi-SNWs in the system.

2.4 Pyrolysis of Gd-SNWs and GdBi-SNWs aerogels

The prepared aerogels were further heat treated at different temperatures under N_2 flow of 50 mL/min in tube furnace. Firstly, the samples were heated to 500 °C at a rate of 2 °C/min and held at that temperature for 1 h. Subsequently, the samples were continued to be heated to 850 °C at a rate of 5 °C/min and held at 850 °C for 1 h. The samples derived from Gd-SNWs aerogels were labeled as Gd-800, Gd-850, and Gd-900 at the pyrolysis temperature of 800, 850, and 900 °C, respectively. The samples derived from GdBi-SNWs aerogels at the pyrolysis temperature of 850 °C were labeled as GdBi1-850 and GdBi2-850.

2.5 Characterization

The microstructures of the aerogel microspheres were observed by scanning electron microscopy (SEM, Thermo Fisher Apreo 2C) and transmission electron microscopy (TEM, Thermo Fisher Talos F200i). X-ray diffraction (XRD) spectroscopic analysis: This experiment used Empyrean type powder XRD to analyze the phase structure of the sample. The analysis conditions are working

current of 40 mA, working voltage of 45 kV, scanning range of 10°–90°, scanning speed of 5°/min, and Cu target conditions. The Raman spectra were collected on a Raman spectrometer (Horiba Scientific LabRAM HR Evolution) equipped with a laser with an excitation wavelength of 532 nm. Fourier transform infrared (FT-IR) spectra were recorded with a PerkinElmer Spectrum 3 in the attenuated total reflection mode. X-ray photoelectron spectroscopy (XPS) spectra were collected on Thermo Scientific K-Alpha. The thermal weight loss of aerogels in air was studied by using the STA449 F3 thermogravimetric analyzer of NETZSCH. The samples were heated from room temperature to 800, 850, and 900 °C at a heating rate of 10 °C/min under a mixed atmosphere of N_2 and O_2.

2.6 Electromagnetic measurements

Electromagnetic parameters for the aerogels were measured with a vector network analyzer (N5234B PNA-X, Agilent) across the frequency range of 2–18 GHz. The measured samples were prepared by immersing the aerogels with paraffin matrix and compacted into toroidal-shaped samples of 7.00 mm outer diameter and 3.04 mm inner diameter.

The values of reflection loss (RL), determined according to transmission line theory and computed from the relative complex permittivity and permeability at specific frequencies and matching thicknesses from Eqs. (1) and (2), were employed to assess electromagnetic wave absorption (EWA) performance

$$\mathrm{RL} = 20\lg|R| = 20\lg\frac{|Z_{\mathrm{in}}-Z_0|}{|Z_{\mathrm{in}}+Z_0|} \tag{1}$$

$$\frac{Z_{\mathrm{in}}}{Z_0} = \left(\frac{\mu_{\mathrm{r}}}{\varepsilon_{\mathrm{r}}}\right)^{1/2}\tan h\left[\frac{2\pi \mathrm{j} f d}{c}\left(\mu_{\mathrm{r}}\varepsilon_{\mathrm{r}}\right)^{1/2}\right] \tag{2}$$

where Z_{in}, Z_0, ε_{r}, μ_{r}, f, c, d, R, tan$h$, and j represent the input impedance of the absorbent, free space impedance, the complex permittivity, permeability, incident EMW frequency, light speed in a vacuum, matching thickness, reflection coefficient, hyperbolic tangent, and imaginary unit, respectively.

In generally, the polarization–relaxation process of electromagnetic wave absorption is evaluated by the Cole–Cole plot. The plot based on modified Debye theory was introduced by the following equations

$$\varepsilon' = \varepsilon_\infty + \frac{\varepsilon_{\mathrm{s}}-\varepsilon_\infty}{1+(2\pi f)^2\tau^2} \tag{3}$$

$$\varepsilon'' = (\varepsilon_{\mathrm{s}}-\varepsilon_\infty)\frac{2\pi f\tau}{1+(2\pi f)^2\tau^2} + \frac{\sigma}{2\pi f\varepsilon_0} = \varepsilon_{\mathrm{p}}'' + \varepsilon_{\mathrm{c}}'' \tag{4}$$

where ε' and ε'' are the real and imaginary components of permittivity (ε), respectively; ε_{s} represents the static permittivity; τ is the polarization relaxation time; ε_∞ is the relative dielectric permittivity at the high-frequency limit; σ is the electrical conductivity; ε_0 is the vacuum permittivity; $\varepsilon_{\mathrm{c}}''$ is conduction loss; $\varepsilon_{\mathrm{p}}''$ is polarization loss. The above two equations can be combined and simplified as below

$$\left(\varepsilon' - \frac{\varepsilon_{\mathrm{s}}+\varepsilon_\infty}{2}\right)^2 + (\varepsilon'')^2 = \left(\frac{\varepsilon_{\mathrm{s}}-\varepsilon_\infty}{2}\right)^2 \tag{5}$$

2.7 Theoretical calculations

To analyze the work function, charge transfer, and density of state, the density functional theory (DFT) calculations were performed using the Vienna *ab initio* simulation package (VASP 6.1) and the visualization of VESTA software. The electron exchange–correlation function was treated using a generalized gradient approximation (GGA) in the form proposed by Perdew, Burke, and Ernzerhof (PBE). Ion–electron interaction was described by the projector augmented-wave (PAW) method. The energy cutoff of the plane waves was set to 500 eV. All presented geometry optimizations were obtained until the maximum displacement below 0.005 Å, energy tolerance below 1×10^{-5} Ha, and the maximum forces lower than 0.01 eV/Å. During the geometry optimizations, the bottom atoms were fixed at the bulk position when the surface properties were calculated. The k-point grid of $3 \times 3 \times 1$ was selected for geometry optimizations, and DFT-D3 was used for van der Waals correction. The (012) surface of Bi and (321) of Gd_2MoO_6 with the vacuum region of about 20 Å along the z-direction were adopted. The isosurface values for the charge density difference is 0.005 e/Å^3, where blue signifies electron accumulation and yellow denotes electron depletion.

3 Results and discussion

3.1 Composition and morphology of the aerogels

The structural evolution of bio-inspired hierarchical architectures using SNWs as building blocks is illustrated in Fig. 1. The Gd-SNWs and Bi-SNWs were synthesized via a hydrothermal method. The as-prepared Gd-SNWs appeared as a white solid, while the Bi-SNWs exhibited a deep cyan color (Fig. S1 in the Electronic Supplementary Material (ESM)). TEM analysis revealed that both products possessed a one-dimensional (1D) wire-like morphology. Subsequently, the synthesized SNWs were dispersed in cyclohexane to form a uniform dispersion for further freeze-casting. The SNWs were self-assembled during the freeze-casting process under the guidance of directionally grown ice templates, forming an aerogel with biomimetic micro/nanostructures after subsequent thermal treatment (Fig. 1(a)). This process constructs two key structural features: first, a honeycomb-like macroporous structure formed on the aerogels (Fig. 1(d)), and second, a well-defined aligned microchannel architecture resembling butterfly wings, observed in the aerogel cross-section (Figs. 1(e)–1(g)). Notably, the cross-sectional structure exhibits anisotropy; the axial frameworks serve as guiding systems for electromagnetic waves, while the radial porous cavities can be regarded as resonant clusters that generate strong coupling and multiple scattering effects.

TEM analysis revealed that as the heat treatment temperature was increased from 200 to 250 and 800 °C (Figs. 1(i)–1(k)), the SNWs inside GdBi progressively underwent aggregation and cleavage. It has been proposed that high temperatures decompose the oleylamine/oleic acid ligands attached to the surface of the SNWs, weakening the hydrogen bonding interactions that help maintain the wire-to-particle architecture [33]. This loss of stabilizing forces is considered to lead to the rapid aggregation of the SNWs, followed by their eventual cleavage. This microstructural evolution directly induced macroscopic volume contraction of the aerogel (Fig. S2 in the ESM). Moreover, the shift of the characteristic peaks in the Fourier-transform infrared spectra (Fig. S4 in the ESM) not only confirmed the effective removal of surface oleylamine/oleic acid ligands but also revealed consequent changes in the chemical environment—particularly the notable

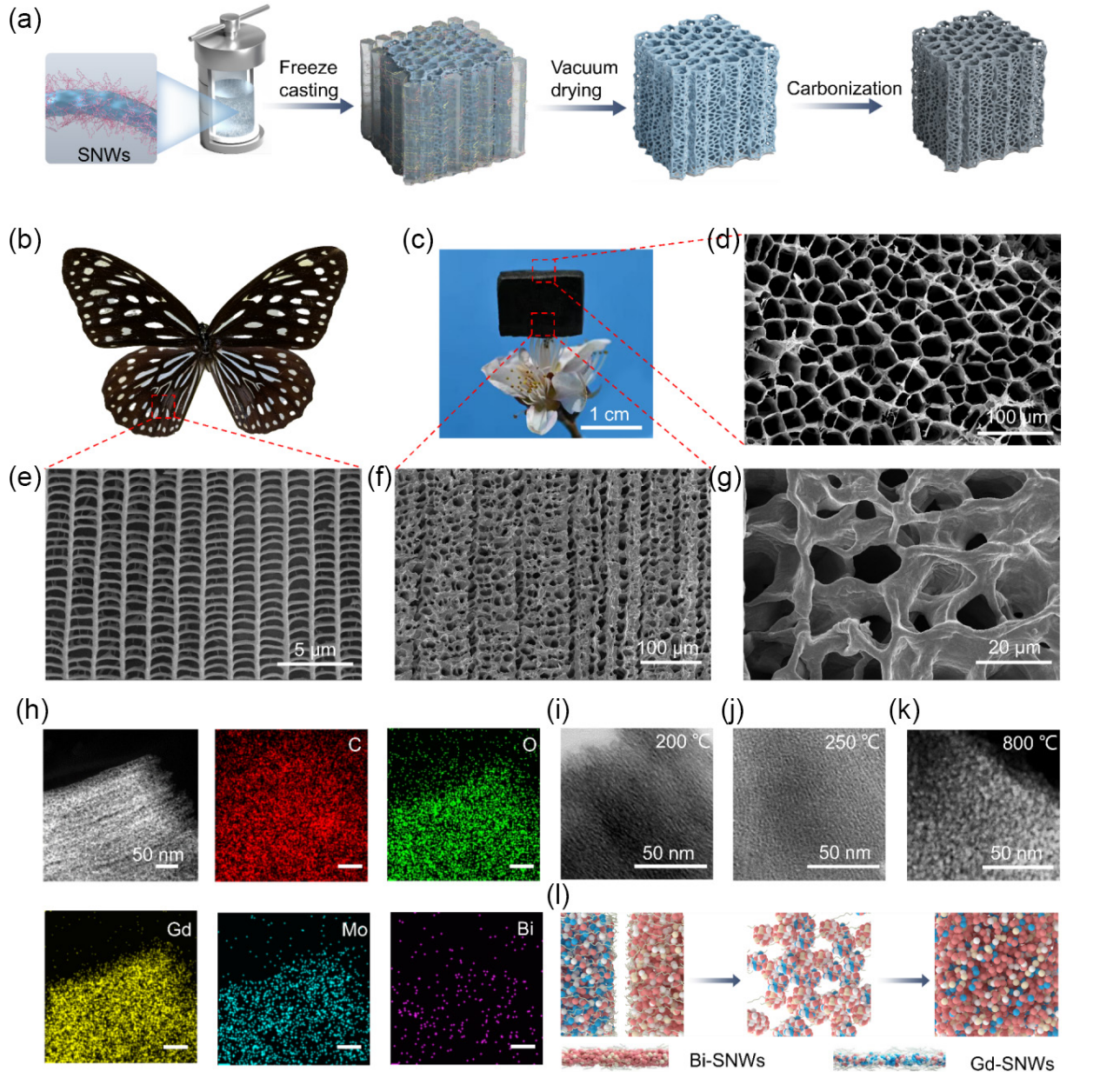


Figure 1 (a) Scheme of the synthetic procedure for the preparation of GdBi-derived aerogels. Optical photographs of (b) butterfly wing and (c) aerogel. SEM images of (d) surface of the aerogel, (e) butterfly wing, and ((f) and (g)) cross-section of the aerogel. (h) TEM image and EDS maps of the aerogel. (i)–(k) TEM images at different pyrolysis temperatures. (l) Schematic of aerogel formation via pyrolysis.

weakening of hydrogen bonding interactions, further supporting the aforementioned hypothesis. Elemental mapping demonstrated the homogeneous distribution of Gd, Mo, and Bi within the material, verifying the construction of a stable heterogeneous structure (Fig. 1(h)). The ordered butterfly-inspired structure enhances the multiple scattering of electromagnetic waves, whereas the cleavage of SNWs generates smaller-sized particles, increasing the number of heterointerfaces and optimizing the dielectric properties of the material. This establishes a foundation for highly efficient electromagnetic wave absorption.

3.2 Chemical structure of GdBi-derived aerogels

The phase compositions of the Gd-850 and GdBi2-850 aerogels were characterized using X-ray diffraction (Fig. 2(a)). Gd-850 shows the characteristic peaks of Gd_2O_3 (PDF#74-1987), whereas GdBi2-850 exhibits diffraction peaks corresponding to Gd_2MoO_6 (PDF#24-0423) and metallic Bi (PDF#85-1330) [34–36]. The X-ray photoelectron spectra revealed the chemical states and bonding characteristics of the samples. The two characteristic peaks of Gd 4d in GdBi at 142.1 and 147.03 eV corresponded to the $4d_{5/2}$ and $4d_{3/2}$ of the Gd^{3+} state, respectively. The presence of Gd_2MoO_6 was further confirmed by the Mo 3d spectrum. The doublet observed at 232.7 and 235.8 eV was assigned to Mo^{6+} $3d_{5/2}$ and Mo^{6+} $3d_{3/2}$, respectively, indicating the Mo^{6+} state in Gd_2MoO_6 (Fig. 2(b)) [37]. The Raman spectra shown in Fig. 2(c) indicate substantial defect concentrations in both materials owing to high I_D/I_G ratios (2.67 for Gd-850 and 2.47 for GdBi2-850). The broader T-band in Gd-850 suggests higher carbon disorder, while Bi incorporation promoted crystalline phase formation, slightly reducing the amorphous content while maintaining a high defect density.

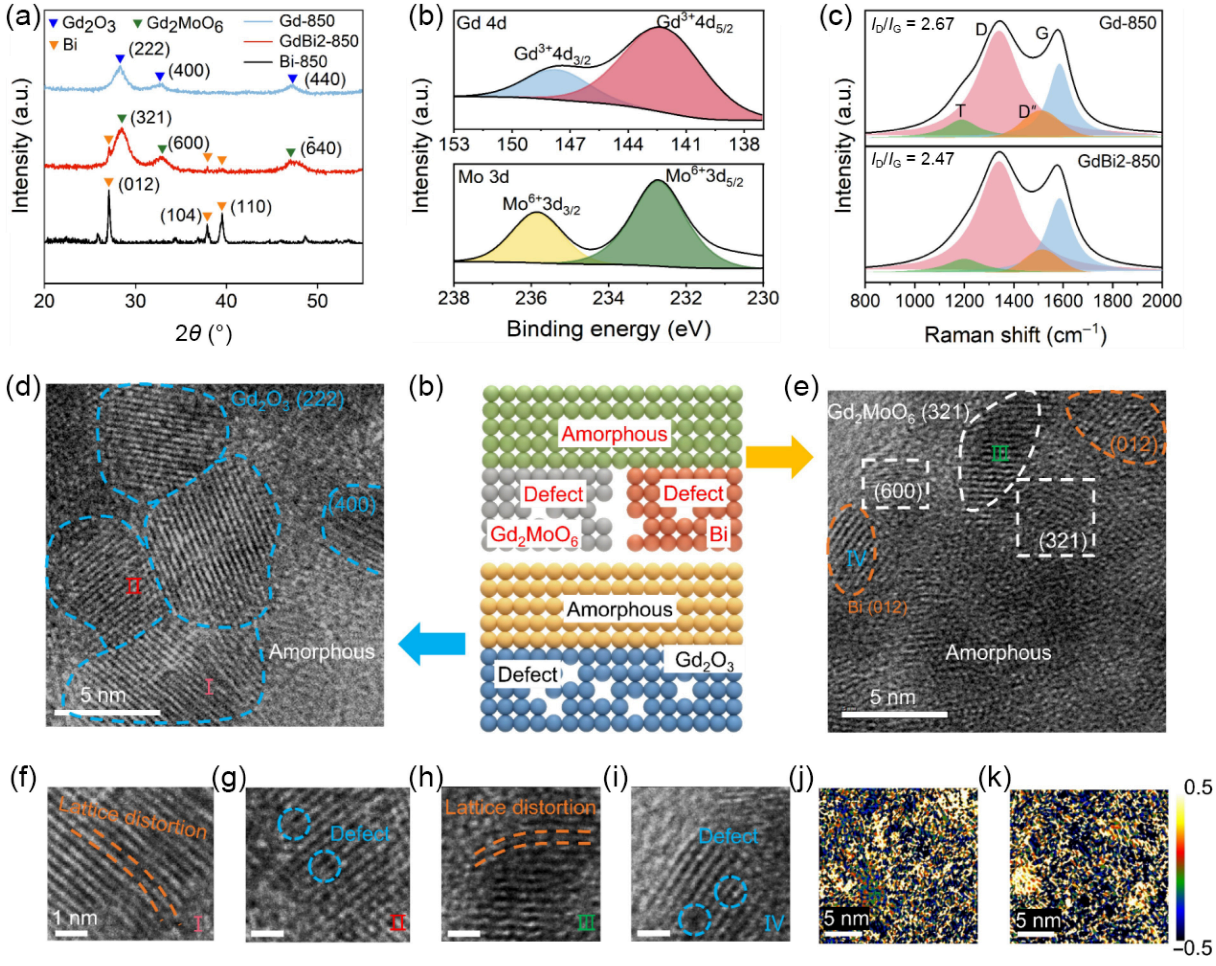


Figure 2 (a) XRD patterns. (b) Mo 3d and Gd 4d XPS spectra of GdBi-850. (c) Raman spectra of the prepared Gd-850 and GdBi2-850. TEM images of (d) Gd-850 and (e) GdBi2-850. (f) and (g) Lattice distortion and defects in Gd-850. (h) and (i) Lattice distortion and defects in GdBi2-850. GPA of (j) Gd-850 and (k) GdBi2-850.

High-resolution TEM (HRTEM) investigations provided deeper microstructural insights. Gd-850 displayed amorphous/crystalline composite regions with lattice defects and distortions (Figs. 2(d), 2(f), and 2(g)), serving as polarization centers. With the incorporation of Bi-SNWs, GdBi-850 developed a more complex architecture featuring crystalline Gd_2MoO_6 and metallic Bi phases (Fig. 2(e)). Lattice spacing measurements confirmed the phase composition, with 0.311 and 0.269 nm corresponding to the (222) plane of Gd_2O_3 in Gd-850, respectively (Fig. S5 in the ESM). Upon the introduction of Bi-SNWs, the microstructure was engineered to form Gd_2MoO_6 (0.311 nm, (321) plane) and metallic Bi (0.327 nm, (012) plane) (Fig. 2(e) and Fig. S6 in the ESM). The intimate contact between Bi and Gd_2MoO_6 established Mott–Schottky heterojunctions, generating BIEFs that enhanced the interfacial polarization [38]. Furthermore, the introduction of Bi induced a higher defect density and stronger lattice strain (Figs. 2(h) and 2(i)), creating additional polarization sites. Geometric phase analysis (GPA) revealed enhanced lattice strain along the ε_{xy} direction in GdBi2-850 (Figs. 2(j) and 2(k)), which synergistically creates abundant polarization centers alongside the high-density defects [39].

3.3 Electromagnetic wave absorption performance

The microwave absorption performances of the as-prepared aerogels were systematically evaluated across different compositions and pyrolysis temperatures. The RL curves of the aerogels were evaluated based on their measured electromagnetic parameters using the transmission line theory (Eqs. (1) and (2)) [37]. Gd-800 demonstrated limited performance with an EAB_{max} of only 4.1 GHz, which was attributed to insufficient dielectric phases and heterointerfaces (Fig. 3(a)). Increasing the pyrolysis temperature significantly enhanced the absorption properties: Gd-850 achieved an excellent EAB_{max} of 7.9 GHz at a thickness of 2.75 mm (Fig. 3(b)), while Gd-900 maintained a wide EAB_{max} of 6.5 GHz at a reduced thickness of 2.00 mm (Fig. 3(c)). The introduction of Bi-SNWs facilitated the formation of Gd_2MoO_6 and Bi during thermal treatment, thereby creating Bi/Gd_2MoO_6 Schottky heterointerfaces. The GdBi2-850 delivered an optimal performance with an EAB_{max} of 8.3 GHz at a thickness of 2.80 mm (Fig. 3(d)). This composition maintained strong absorption across the 2.80–4.00 mm thickness range, fully covering the entire Ku-band (12–18 GHz). However, further increasing the Bi-SNWs content (GdBi1-850) degraded performance, reducing the RL_{min} to −19.5 dB and EAB_{max} to 6.4 GHz (Fig. 3(f)). A comparative analysis revealed that both Gd- and GdBi-derived aerogels could achieve broad bandwidths at lower thicknesses, outperforming numerous reported aerogel absorbers including graphene [40, 41], MXene [42], polymer [43], and carbon [44–49] systems (Fig. 3(g) and Table S1 in the ESM). When applied as layers over a perfect electric conductor, both Gd-850 and GdBi2-850 significantly reduced the reflected radar signals, with GdBi2-850 exhibiting the strongest attenuation

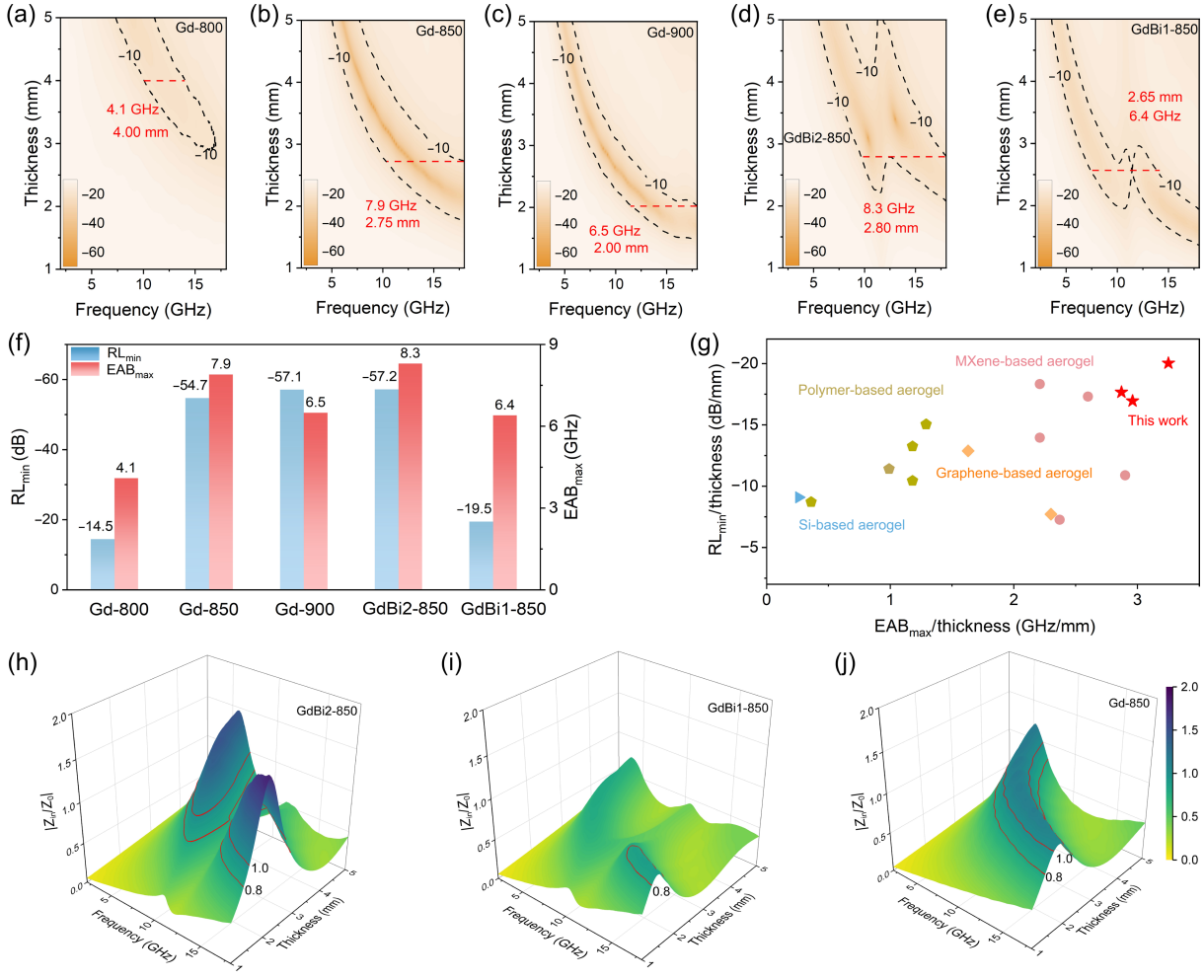


Figure 3 Microwave absorption performance of Gd and GdBi-derived aerogels. (a)–(e) 2D plots of RL values. (f) Comparison chart of RL_{min} and EAB_{max} for the above samples. (g) Comparison of the microwave absorption performance (RL_{min}/thickness and EAB_{max}/thickness) between Gd-850, GdBi2-850, and previously reported microwave absorbers. 3D plots of $|Z_{in}/Z_0|$ of (h) GdBi2-850, (i) GdBi1-850, and (j) Gd-850.

characteristics (Fig. S7 in the ESM). The minimal reflected signals across virtually the entire detection range demonstrated highly efficient electromagnetic energy dissipation, validating the experimental results and confirming that optimal Bi-SNWs incorporation effectively enhanced the microwave absorption capability.

3.4 Electromagnetic response behavior

Analysis of the complex permittivity ($\varepsilon_r = \varepsilon' - j\varepsilon''$) and permeability ($\mu_r = \mu' - j\mu''$, where μ' and μ'' are the real and imaginary parts, respectively) of all samples revealed a marked contrast in their frequency response. The ε' and ε'' components of permittivity displayed strong frequency-dependent variations, whereas the corresponding components of permeability (μ' and μ'') showed a relatively weak dependence on frequency [50]. The ε' and ε'' values of the heterostructured aerogel decreased with increasing frequency, which can be attributed to polarization lag at higher frequencies (Figs. 4(a) and 4(b)) [51]. Notably, temperature significantly influenced the dielectric constant. During heat treatment, the organic ligands on sub-1 nm nanowires carbonize, with higher temperatures yielding greater carbon content and thus enhancing conductive loss. As the frequency of the electromagnetic wave increases from 2 to 18 GHz, the ε' values of Gd-800, Gd-850, Gd-900 decreased from 4.81 to 2.78, 8.26 to 3.92, and 10.43 to 6.43, respectively, with the ε'' values changing from 2.06 to 0.88, 2.71 to 2.95, and 3.2 to 4.04, respectively. Therefore, both the ε' and ε'' values of the samples increased with increasing pyrolysis temperature. According to the free electron theory, the increase in the dielectric constant is closely related to the enhanced electrical conductivity caused by increased graphitization [52]. For Gd-900, the higher dielectric constant tends to induce a skin effect on the surface, leading to impedance mismatch. The comparison of the ε', ε'', and $\tan\delta_\varepsilon$ curves of Gd-800, Gd-850, and Gd-900 revealed that the broad-frequency dielectric effect triggered by the heterogeneous nanodomains was more pronounced at a pyrolysis temperature of 850 °C (Fig. 4(c)).

To investigate the dielectric loss mechanism, ε'' can be decomposed into ε_c'' and ε_p''. The increase in ε_c'' is positively correlated with enhanced conductivity (Figs. 4(d)–4(f)). As the frequency increased, ε_c'' gradually decreased, which can be explained by the weakening of conduction loss at high frequencies. In addition to the relaxation peak of Gd-850 (Fig. 4(d)), the presence of notable multi-frequency fluctuations within the 10–12 GHz range for the GdBi2-850 and GdBi1-850 samples (Figs. 4(e) and 4(f)) indicated enhanced polarization relaxation processes. This confirmed that the introduction of Bi-SNWs

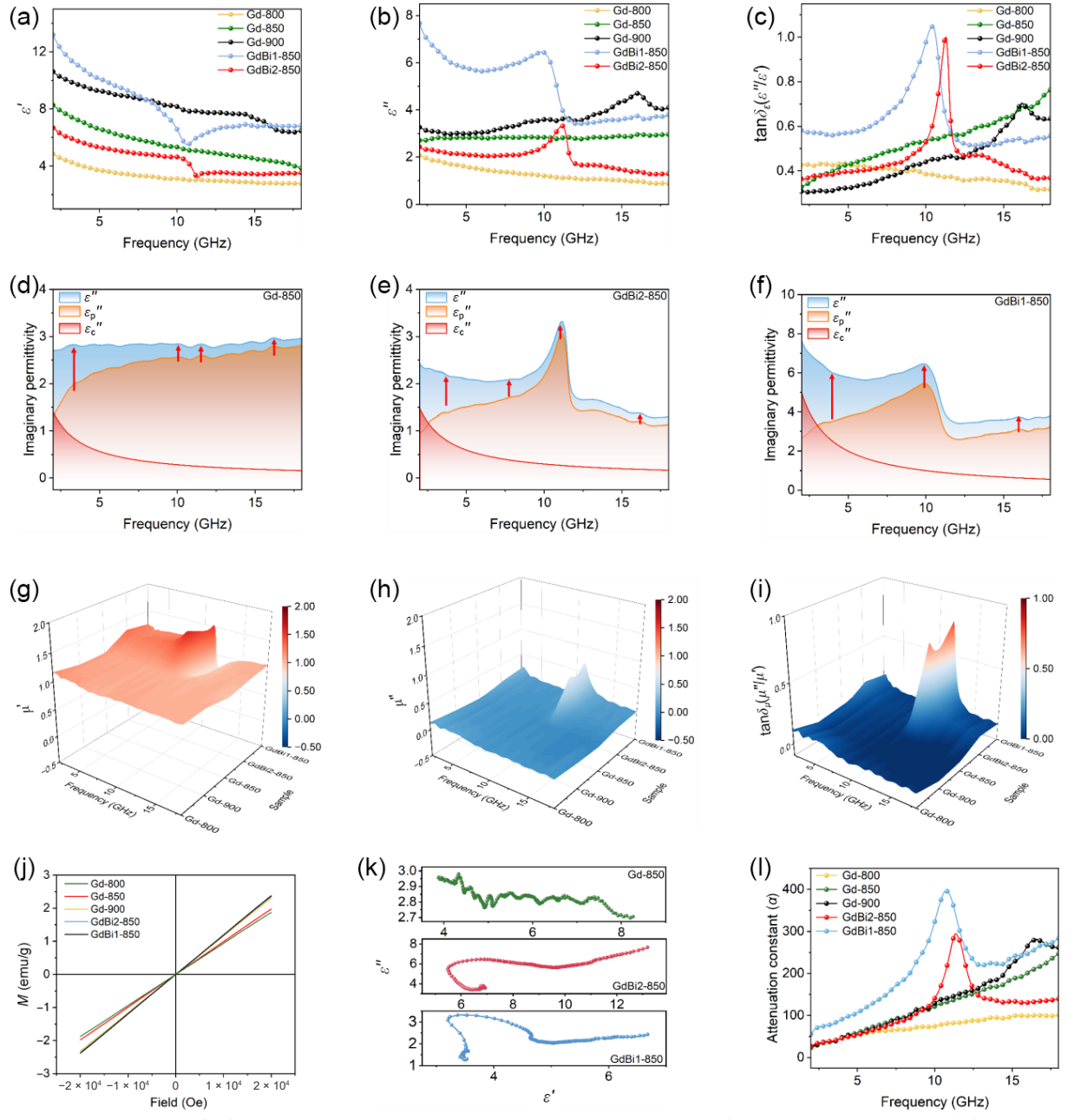


Figure 4 (a) ε', (b) ε'', and (c) $\tan\delta_\varepsilon$ of Gd-800, Gd-850, Gd-900, GdBi1-850, and GdBi2-850. ε, ε_c'', and ε_p'' of (d) Gd-850, (e) GdBi2-850, and (f) GdBi1-850. (g) μ', (h) μ'', and (i) $\tan\delta_\mu$ of permeability of Gd-based subnanowire aerogel (GdSnwA) and Gd-based/Bi-based subnanowire composite aerogel (GdBiSnwA). (j) Hysteresis loops for Gd-800, Gd-850, Gd-900, GdBi2-850, and GdBi1-850. (k) Cole–Cole plots of Gd-850, GdBi2-850, and GdBi1-850. (l) α of Gd-800, Gd-850, Gd-900, GdBi2-850, and GdBi1-850.

significantly increased the contribution of the dielectric polarization loss to the dielectric attenuation mechanism.

In addition, the introduction of Bi-SNWs leads to the formation of Bi within GdBi samples after heat treatment, which enhances the electrical conductivity of the material and intensifies the conduction loss. However, as the content of Bi-SNWs further increased, the electromagnetic wave absorption performance of GdBi1-850 actually declined. This decline is mainly attributed to the severe impedance mismatch caused by the excessively high electrical conductivity, which leads to most of the electromagnetic waves being reflected at the material's surface and unable to penetrate into the interior for effective dissipation. In terms of magnetism, as shown in Figs. 4(g)–4(i), the μ' values of the Gd samples fluctuate around 1.0, while the μ'' values are close to 0, indicating that their magnetic property is extremely weak and can be ignored. In contrast, both the μ' and μ'' values of the GdBi samples are higher than those of the Gd samples, suggesting that the introduction of Bi-SNWs endows the material with considerable magnetic properties. In its single-phase structure of Gd_2MoO_6, there is a small amount of mixed valence states of Mo^{4+} and Mo^{6+}, among which the presence of paramagnetic Mo^{4+} ions contributes to the overall magnetic moment of the system. The hysteresis loops show that all samples are linear curves without hysteresis, indicating that the material as a whole exhibits paramagnetism (Fig. 4(j)). This further confirms that the Gd_2MoO_6 phase is an important source of paramagnetism in the GdBi aerogel [53].

Dielectric polarization loss is influenced by the Debye relaxation process, which can be characterized using Cole–Cole semicircular curves (Fig. 4(k)). When Debye relaxation occurs in a material, the Cole–Cole curve exhibits a distorted semicircular shape. The profiles of Gd-850 and GdBi2-850 contained multiple semicircles, suggesting that multiple relaxation processes contributed to their significant polarization loss. The microwave absorption performance of the heterostructured aerogel is closely related to the attenuation constant (α) and impedance matching ($|Z_{in}/Z_0|$) [54, 55]. The α value for all composites increased with frequency, indicating stronger electromagnetic wave attenuation at higher frequencies. Figure 4(l) shows that GdBi1-850 has the highest α value, yet its microwave absorption performance is not optimal. Although GdBi2-850 had a lower α value than GdBi1-850, it exhibited better absorption performance, which can be mainly attributed to its favorable impedance matching characteristics. Good impedance matching allows electromagnetic waves to penetrate the material more effectively, thereby enhancing energy dissipation. The degree to which $|Z_{in}/Z_0|$ approaches 1 is generally used as the criterion for evaluating the impedance-matching capability: Values closer to 1 over a broader frequency band indicate more satisfactory matching (Figs. 3(h)–3(j)). Therefore, the excellent microwave absorption performance of GdBi2-850 results from the synergistic effect of its moderate electromagnetic attenuation capability and its optimal impedance matching properties.

3.5 Electromagnetic wave absorption mechanism

The unique cross-grating microstructure of butterfly wings, specifically their ridge arrays and vertically intersecting ribs forming primary and secondary diffraction surfaces, respectively, synergistically enhances the ability to manipulate light of specific wavelengths through multi-level diffraction. The interstitial pore structures create a gradient refractive index layer, significantly reducing surface reflectance. This intricate biophotonic structure is a crucial source of inspiration for the innovative design of graded porous aerogels. By biomimetically constructing multi-level diffraction structures within the GdBi aerogel and synergistically integrating polarization loss layers composed of heterogeneous nanodomains, effective coordination between electromagnetic wave absorption and surface reflection reduction has been achieved. GdBi2-850 exhibits excellent electromagnetic absorption performance, which is attributed to its butterfly-inspired hierarchical porous structure. The abundant pores allow electromagnetic waves to undergo additional scattering at large angles of incidence, functioning as resonant cavities that distort the electromagnetic field near their surface and thus generating multiple oscillations and diffraction effects. The introduction of Bi-SNWs enhanced the conductivity of the inner pore walls, thereby dissipating electromagnetic wave energy through conduction loss (Fig. 5(a)). In addition, the heterophase interface formed between the crystalline and amorphous phases minimized the redistribution of the interfacial charge. This reduction in the accumulated charge on both sides lowers the interface barrier, allowing electrons to migrate more readily and thereby enhancing conductive loss. The introduction of Bi-SNWs provides the material with magnetic loss characteristics. This magnetic loss works in synergy with multiple scattering loss and dielectric loss, and together they exert a significant effect, enabling the material to efficiently absorb electromagnetic waves.

Moreover, when the metal conductor Bi comes into contact with the semiconductor Gd_2MoO_6, the work function difference between Bi (Φ = 4.57 eV) and Gd_2MoO_6 (Φ = 5.30 eV) is 0.73 eV (Figs. 5(b) and 5(c)). This energy difference provides the core driving force for directional electron migration, ultimately forming a stable BIEF. This field significantly reduced the reconstruction energy barrier. Driven by the BIEF, electrons migrate directionally, causing the metallic Bi to lose electrons and become an electron-deficient region, while the semiconductor Gd_2MoO_6 gains electrons and becomes an electron-rich region (Fig. 5(d)). The detailed mechanism is explained as follows (Fig. 5(e)). The Fermi level of Gd_2MoO_6 is typically located near the middle of its bandgap, lower than that of Bi. When Bi and Gd_2MoO_6 come into contact, their Fermi levels must align to reach equilibrium. To achieve this, electrons flow from the material with the higher Fermi level (Bi) to the one with the lower Fermi level (Gd_2MoO_6). This flow continued until the Fermi levels were aligned at the interface. The electrons transferring from Bi naturally occupy the lowest available empty states in Gd_2MoO_6, which are located at the bottom of the conduction band (Fig. 5(f)). This process confirms the presence of an enhanced charge-transfer mechanism at the heterointerface, characterized by a BIEF and a space-charge region. These phenomena significantly promote interface polarization and modulate conduction loss (Fig. 5(g)). In addition, the presence of Gd_2MoO_6 endows the GdBi samples with certain magnetism, contributing to magnetic loss under electromagnetic wave exposure (Fig. 4(j)). The synergistic effect of dielectric loss and magnetic loss collectively enhances the electromagnetic wave absorption and shielding performance of GdBi2-850.

4 Conclusions

Inspired by the architecture of butterfly wings, heterostructured aerogels (GdBi2-850) containing Schottky heterointerfaces were fabricated via freeze casting and thermal treatment. The constructed Bi/Gd_2MoO_6 Schottky heterointerfaces enhanced its dielectric contrast and created BIEFs through interfacial chemical bonding, which substantially promoted the dissipation of electromagnetic waves. The locally asymmetric atomic arrangements at these interfaces formed polarized atomic pairs, effectively modulating electron distribution and activating dipole polarization. Furthermore, high-density grain boundaries induced lattice distortions and discontinuous crystal fringes, significantly contributing to dielectric polarization. This study provides insights for designing heterointerface-rich absorbing materials and proposes a strategic approach for developing high-performance electromagnetic energy attenuation systems based on sub-1 nm nanomaterials, underscoring their potential for practical electromagnetic protection applications.

Electronic Supplementary Material: Supplementary material (Figs. S1–S7 and Table S1, covering TEM images, shrinkage rates, TGA/FTIR data, lattice measurement, 3D RCS plots, and reported microwave absorption performance) is available in the online version of this article at https://doi.org/10.26599/NR.2026.94908689.

Data availability

The data that support the findings of this study are available from the corresponding author upon reasonable request.

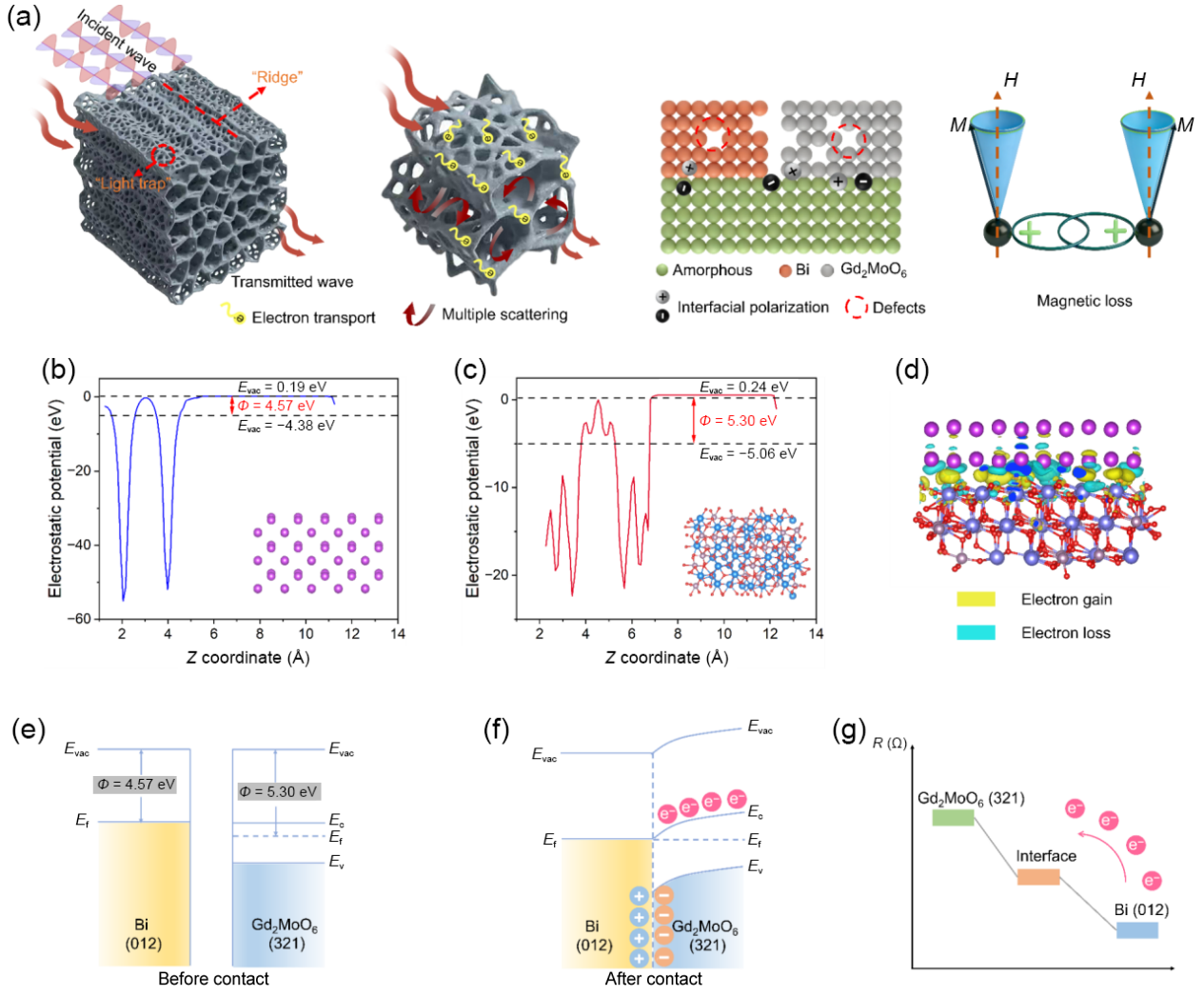


Figure 5 (a) Diagram of electromagnetic wave absorption mechanism. The work function of (b) Bi (012) and (c) Gd_2MoO_6 (321). (d) Differential charge density between Bi (012) and Gd_2MoO_6 (321) along the *a*–axis. (e) Energy band alignment and (f) resistance change of Bi (012) and Gd_2MoO_6 (321) heterojunction before and after Schottky contact. (g) Resistance change of the Gd_2MoO_6(321)/Bi(012) heterojunction before and after Schottky contact.

Acknowledgements

This work was supported by the Natural Science Foundation of Inner Mongolia (No. 2025YQ047), the National Natural Science Foundation of China (Nos. 52164013 and 22466028), Young Elite Scientists Sponsorship Program by Jiangsu Association for Science and Technology (No. JSTJ2023XH047), and China Postdoctoral Science Foundation (No. 2025T180037).

Declaration of competing interest

All the contributing authors report no conflict of interests in this work.

Author contribution statement

T. Z.: Data curation, validation, writing manuscript, experimental design. B. Q. B.: Data curation, validation, experimental design. Y. X. D.: Data curation, validation, experimental design. G. F. S.: Project administration, funding acquisition. R. F.: Project administration, funding acquisition. H. Z. S.: Project administration, funding acquisition.

Use of AI statement

None.

References

[1] Zong, J. Y.; Zhai, H. Z.; Guan, H. Z.; Wang, Z. Z.; Cao, M. S.; Cao, W. Q. Host–guest engineered electromagnetic fabrics with controllable polarization–conduction network for multispectral stealth and wireless actuation. *Adv. Funct. Mater.* **2025**, *35*, e07277.

[2] Hao, B.; Zhang, Y.; Si, H. X.; Jiang, Z. Y.; Li, C. P.; Zhang, Y. B.; Zhang, J. W.; Gong, C. H. Multiscale design of dielectric composites for enhanced microwave absorption performance at elevated temperatures. *Adv. Funct. Mater.* **2025**, *35*, 2423897.

[3] Zhao, P. Y.; Peng, H. L.; Cai, B.; Zhou, L.; Liang, C. M.; Koo, M. C.; Wang, H. Y.; Wu, J. T.; Hou, Z. L.; Wang, G. S. Mechanism decoupling of impedance matching and attenuation enhancement via spatial distribution of loading components. *Adv. Funct. Mater.* **2026**, *36*, e18479.

[4] Jiang, X. W.; Wang, Q.; Song, L. M.; Lu, H. X.; Xu, H. L.; Shao, G.; Wang, H. L.; Zhang, R.; Wang, C. G.; Fan, B. B. Enhancing electromagnetic wave absorption with core–shell structured SiO_2@MXene@MoS_2 nanospheres. *Carbon Energy* **2024**, *6*, e502.

[5] Liang, J.; Zhu, S. Y.; Chen, D. W.; Li, Y. J.; Zhou, D.; Meng, N.;

Liao, Y. Z.; Sun, H. X.; Kong, J. Dual built-in electric field engineering in heterostructure nickel–cobalt bimetallic composites for boosted electromagnetic energy dissipation. *Adv. Powder Mater.* **2025**, *4*, 100344.

[6] Liu, Y.; Wang, K.; Xu, X. T.; Eid, K.; Abdullah, A. M.; Pan, L. K.; Yamauchi, Y. Recent advances in faradic electrochemical deionization: System architectures versus electrode materials. *ACS Nano* **2021**, *15*, 13924–13942.

[7] Zhou, J. J.; Zhang, Y. K.; Wang, X. Y.; Yang, Y. N.; Wu, X.; Hu, J.; Xia, L. Coaxial $Al_4C_3/Al_2O_3@C_f$ composite with tunable core–shell architecture for synergistic electromagnetic absorption and thermal insulation. *Compos. Part B: Eng.* **2025**, *306*, 112830.

[8] Tao, Z.; Gu, W. H.; Tan, X.; Zhang, H. Y.; Wu, C.; Xia, A. L.; Ji, G. B. Carbon materials: A crucial component within the family of high-performance microwave absorbing materials. *Adv. Funct. Mater.* **2025**, *35*, e10644.

[9] Zeng, X. J.; Peng, X. W.; Liu, Q.; Xie, N. H.; Zhang, X. F.; Lu, J.; Gao, Y. F. BiM@NC (M = Fe, Co, Ni; NC = N-doped carbon) nanoplates confined in wood-derived carbon with excellent electromagnetic wave absorption performance. *Adv. Funct. Mater.* **2026**, *36*, e16772.

[10] Li, N.; Zong, Z.; Zhang, F.; Shi, J. F.; Li, Z. Y.; Xu, H. K.; Zhang, Y. F.; Chen, Y. M.; Lei, J.; Xu, L. et al. Barium ferrite with high anisotropy for ultra-broadband microwave absorption. *Adv. Funct. Mater.* **2025**, *35*, 2414694.

[11] Luo, G. T.; Zhu, Y. L.; Chen, P. G.; Chen, F.; Li, X. C.; Che, R. C. Electromagnetic attenuation of Sm-doped alloys modified by interface exchange coupling and magnetocrystalline stress anisotropy. *Adv. Funct. Mater.* **2025**, *35*, 2425298.

[12] Yang, S. Y.; Zang, B. W.; Xiang, M. L.; Shen, F. Y.; Song, L. J.; Gao, M.; Zhang, Y.; Huo, J. T.; Wang, J. Q. Designing Fe-based amorphous alloys with both ultra-high magnetization and ultra-low coercivity through artificial intelligence. *Adv. Funct. Mater.* **2025**, *35*, 2425588.

[13] Wang, S. J.; Zhang, X.; Hao, S. Y.; Qiao, J.; Wang, Z.; Wu, L. L.; Liu, J. R.; Wang, F. L. Nitrogen-doped magnetic-dielectric-carbon aerogel for high-efficiency electromagnetic wave absorption. *Nano-Micro Lett.* **2024**, *16*, 16.

[14] Peng, Q. G.; Yu, W. L.; Gao, C.; Geng, L. L.; Fatehi, P.; Wang, S. J.; Kong, F. G. The synergistic effect of hybridization-micro/nano-structural design on the $Ti_3C_2T_x$ MXene@CoFe-MOF@chitosan heterojunction enhances the absorption of electromagnetic waves. *Adv. Compos. Hybrid Mater.* **2025**, *8*, 232.

[15] Bai, J. L.; Xie, Z. C.; Zhang, P. F.; Wang, S. C.; Liu, Z. H.; Yao, X. M.; Liu, X. J.; Huang, Z. R. Porous $SiCN_{nw}/C/Si_3N_4$ ceramics with controlled component and structure for electromagnetic wave absorption. *Compos. Part B: Eng.* **2025**, *294*, 112164.

[16] Gai, L. X.; Chen, Y. Z.; Wang, Y.; Han, X. J.; Xu, P.; Du, Y. C. Engineering impedance-matched double-shells in hollow Co/carbon microspheres with gradient graphitization for high-efficiency electromagnetic wave absorption. *J. Adv. Ceram.* **2025**, *14*, 9221212.

[17] Pan, F.; Cai, L.; Shi, Y. Y.; Dong, Y. Y.; Zhu, X. J.; Cheng, J.; Jiang, H. J.; Wang, X.; Jiang, Y. F.; Lu, W. Heterointerface engineering of β-chitin/carbon nano-onions/Ni–P composites with boosted Maxwell–Wagner–Sillars effect for highly efficient electromagnetic wave response and thermal management. *Nano-Micro Lett.* **2022**, *14*, 85.

[18] Meena, R.; Dhaka, R. S. Structural and electrical transport properties of NASICON type $Na_3Zr_{2-x}Ti_xSi_2PO_{12}$ (x = 0.1–0.4) solid electrolyte materials. *Small* **2025**, *21*, 2501197.

[19] Portes, R. C.; Lopes, B. H. K.; Rezende, M. C.; Amaral-Labat, G.; Baldan, M. R. Enhancing metacomposite properties and electromagnetic interference shielding: Exploring the interplay between manufacturing processability of carbon fiber elastomeric composite and permittivity/permeability effects. *Adv. Compos. Hybrid Mater.* **2024**, *7*, 208.

[20] Xu, C. Y.; Liu, P. B.; Wu, Z. C.; Zhang, H. B.; Zhang, R. X.; Zhang, C.; Wang, L.; Wang, L. Y.; Yang, B. T.; Yang, Z. Q. et al. Customizing heterointerfaces in multilevel hollow architecture constructed by magnetic spindle arrays using the polymerizing–etching strategy for boosting microwave absorption. *Adv. Sci.* **2022**, *9*, 2200804.

[21] Zheng, J. W.; Zheng, J. W.; Zhang, X. Q.; Yue, P. F.; Cai, W.; Chen, H. B.; Qiao, L.; Ying, Y.; Yu, J.; Li, J. et al. Microwave absorption properties and characterization of porous permanent/soft magnetic composite iron nitride with heterogeneous interfaces. *Adv. Funct. Mater.* **2025**, *35*, 2424988.

[22] Zhang, S.; Liu, X. H.; Jia, C. Y.; Sun, Z. S.; Jiang, H. W.; Jia, Z. R.; Wu, G. L. Integration of multiple heterointerfaces in a hierarchical 0D@2D@1D structure for lightweight, flexible, and hydrophobic multifunctional electromagnetic protective fabrics. *Nano-Micro Lett.* **2023**, *15*, 204.

[23] Ji, S. J.; Qin, M. F.; Zhao, J.; Dai, H. D.; Li, J. J. Biomimetic water-based metamaterial absorber for ultrabroadband radar stealth. *Adv. Mater.* **2026**, *38*, e07439.

[24] Wang, H. Y.; Hu, P. F.; Sun, X. B.; Hou, Z. L.; Zhao, P. Y.; Zhou, L.; Yang, S. H.; Geng, C. Y.; Zhu, Y. F.; Wu, X. J. et al. Bioinspired disordered aerogel for omnidirectional terahertz response. *Adv. Mater.* **2025**, *37*, 2418889.

[25] Sansone, N. D.; Aguiar, R.; Embabi, M.; Cheung, N.; Tuccitto, A. V.; Chang, N. R. S.; Leroux, M.; Lee, P. C. Butterfly-inspired hierarchical hybrid composites for lightweight structural thermal management applications. *Adv. Funct. Mater.* **2025**, *35*, 2420744.

[26] Yang, M. Z.; Yuan, F.; Shi, W. X.; Ren, W. B.; Guo, M. F.; Ouyang, C.; Zhou, L.; Sun, N. N.; Xiao, Y.; Xu, E. X. et al. Sub-nanowires boost superior capacitive energy storage performance of polymer composites at high temperatures. *Adv. Funct. Mater.* **2023**, *33*, 2214100.

[27] Liu, Q. D.; Wang, X. Y.; Wang, X. Sub-1 nm materials chemistry: Challenges and prospects. *J. Am. Chem. Soc.* **2024**, *146*, 26587–26602.

[28] Ni, B.; Shi, Y. A.; Wang, X. The sub-nanometer scale as a new focus in nanoscience. *Adv. Mater.* **2018**, *30*, e1802031.

[29] Zhang, S. J.; Zheng, J. J.; Zhao, Z. W.; Du, S. X.; Lan, D.; Gao, Z. G.; Wu, G. L. New prospects in built-in electric fields for electromagnetic wave absorption: From fundamentals to interdisciplinary applications. *Adv. Funct. Mater.* **2026**, *36*, e13762.

[30] Shao, G. F.; Hanaor, D. A. H.; Shen, X. D.; Gurlo, A. Freeze casting: From low-dimensional building blocks to aligned porous structures—A review of novel materials, methods, and applications. *Adv. Mater.* **2020**, *32*, 1907176.

[31] Zhang, S. M.; Lin, H. F.; Yang, H. Z.; Ni, B.; Li, H. Y.; Wang, X. Highly flexible and stretchable nanowire superlattice fibers achieved by spring-like structure of sub-1 nm nanowires. *Adv. Funct. Mater.* **2019**, *29*, 1903477.

[32] Zhang, S. M.; Shi, H. D.; Tang, J. W.; Shi, W. X.; Wu, Z. S.; Wang, X. Super-aligned films of sub-1 nm Bi_2O_3-polyoxometalate nanowires as interlayers in lithium-sulfur batteries. *Sci. China Mater.* **2021**, *64*, 2949–2957.

[33] Du, Y. X.; Liu, D.; Du, R.; Xiu, Y. Y.; Fu, R.; Yang, X.; Liu, L. P.; Sai, H. Z. Sub-1 nm nanowire aerogels. *Adv. Funct. Mater.* **2025**, *35*, 2413651.

[34] Ye, J. Q.; Ge, T. C.; Qu, X.; Mohideen, M. M.; Wang, C.; Hu, P.; Liu, Y. Spatial and electrostatic dual-confinement in hierarchical hollow Bi-Bi_2O_3@carbon nanofibers for dendrite suppression and side reaction mitigation in aqueous zinc-ion batteries. *Adv. Funct. Mater.* **2025**, *35*, 2425358.

[35] Wu, Y. S.; Wang, H. Q.; Xiao, F. S.; Wu, Z. B. Gadolinium-mediated

oxygen affinity induced efficient covalorization of CH_4 and N_2O in an Ir–Gd_2O_3 single-atom catalyst. *J. Am. Chem. Soc.* **2025**, *147*, 25787–25798.

[36] Kumaravel, S.; Devarayapalli, K. C.; Kim, B.; Lim, Y.; Lee, D. S. MXene-boosted MOF-derived hierarchical porous C, N-doped In_2O_3/Gd_2MoO_6 heterostructures with rich oxygen vacancies enable highly efficient bifunctional electrocatalysts for water/seawater electrolysis. *J. Mater. Sci. Technol.* **2026**, *247*, 130–148.

[37] Li, X. M.; Xu, S. K.; Zhang, Z. F.; Yu, Z. Q.; Pan, Z. D.; Yang, Y. J.; Lu, X. B.; Huo, N. J. Controllable growth of MoO_3 dielectrics with sub-1 nm equivalent oxide thickness for 2D electronics. *Nat. Commun.* **2025**, *16*, 6758.

[38] Yu, G. Y.; Shao, G. F.; Xu, R. P.; Chen, Y.; Zhu, X. H.; Huang, X. G. Metal–organic framework-manipulated dielectric genes inside silicon carbonitride toward tunable electromagnetic wave absorption. *Small* **2023**, *19*, 2304694.

[39] He, Y. F.; Liu, D. D.; Dou, S. H.; Ma, L.; Dan, Z. Y.; Yang, M. H.; Zhong, B.; Xia, L.; Huang, X. X. Interface-engineered decoupled conductivity and relaxation: Synergistic modulation of Debye-parameters in N-doped SiO_2/MXene broadband wave-absorbing materials. *J. Adv. Ceram.* **2025**, *14*, 9221150.

[40] Su, Q.; He, Y. F.; Liu, D. D.; Li, D. G.; Xia, L.; Huang, X. X.; Zhong, B. Facile fabrication of graphene/g-C_3N_4 for electromagnetic wave absorption. *Nano Res.* **2024**, *17*, 1687–1698.

[41] Meng, F. B.; Wang, H. G.; Wei, W.; Chen, Z. J.; Li, T.; Li, C. Y.; Xuan, Y.; Zhou, Z. W. Generation of graphene-based aerogel microspheres for broadband and tunable high-performance microwave absorption by electrospinning-freeze drying process. *Nano Res.* **2018**, *11*, 2847–2861.

[42] Dai, B.; Ma, Y.; Dong, F.; Yu, J.; Ma, M. L.; Thabet, H. K.; El-Bahy, S. M.; Ibrahim, M. M.; Huang, M. N.; Seok, I. et al. Overview of MXene and conducting polymer matrix composites for electromagnetic wave absorption. *Adv. Compos. Hybrid Mater.* **2022**, *5*, 704–754.

[43] Xu, Y.; Tan, R. Y.; Jiang, X. L.; Bo, L. W.; Wang, Y. D.; Xu, H. C.; Chen, P.; Xi, K. Hierarchical composite polyimide aerogels with hyperbranched siloxane for high electromagnetic wave absorption. *Adv. Funct. Mater.* **2025**, *35*, 2421389.

[44] Nie, W. B.; Wang, B. J.; Wu, W.; Li, S. K.; Huang, F. Z.; Ma, W. L.; Zhang, H. *In situ* growth medium entropy alloy nanoparticles on the ordered structure carbon nanofiber aerogel for enhanced microwave absorption and infrared stealth properties. *Small* **2025**, *21*, 2503955.

[45] Liu, Q.; Zhang, L. L.; Wan, X. Y.; Song, B. S.; Yan, Z. C.; Li, S.; Yin, X. M.; Ren, X. R.; Li, H. J. Robust and thermostable silicon-based aerogels towards highly efficient thermal insulation and microwave absorption. *J. Mater. Sci. Technol.* **2026**, *257*, 222–232.

[46] Han, X. J.; Feng, Y. F.; Zhang, N.; Du, W.; Zhang, W. L.; Yu, Q. Q.; Liu, Y. F.; Wang, B.; Jiang, F. Y.; Liu, L. Y. et al. Bio-based multifunctional carbon aerogels for ultrawide electromagnetic wave absorption and thermal insulation. *Carbon* **2025**, *238*, 120231.

[47] Long, H.; Qian, Y. X.; Gang, S. F.; Zhang, W. G.; Yang, B. Y.; Wei, Y. C.; Wang, B.; Li, W.; Jiang, Q. H. High-performance thermoelectric composite of Bi_2Te_3 nanosheets and carbon aerogel for harvesting of environmental electromagnetic energy. *ACS Nano* **2025**, *19*, 1819–1831.

[48] Wang, A. P.; Zhang, Z. C.; Liu, Y. J.; Li, Z. B.; Leng, J. S. Lightweight carbon nanotube/aramid nanofiber aerogel with superior electromagnetic wave absorption, thermal insulation, and flame resistance. *Carbon* **2024**, *225*, 119105.

[49] Lin, X.; Wang, C. C.; Zhang, C. Q.; Guo, Q.; Hu, C. S.; Yang, Y.; Zhou, Y. H.; Lin, X. Y.; Zhang, W. W.; Xu, J. T. Asymmetric gradient-structured PPy@bacterial nanocellulose aerogels enable broadband microwave absorption via synergistic polarization-conduction loss. *Chem. Eng. J.* **2025**, *520*, 166529.

[50] Jiang, J. J.; Deng, X. M.; Li, S. H.; Zeng, X. J.; Wu, C. X.; Yang, C. Hierarchically porous multiphase Si-based ceramics with synergistic electromagnetic wave absorption mechanisms. *Adv. Sci.* **2025**, *12*, e10445.

[51] Chen, Y. K.; Wang, X. Q.; Cui, W. G.; Gao, Y.; Pan, H. G.; Wang, Y.; Che, R. C. Multiple Schottky contacts motivated via defects to tune the response ability of electromagnetic waves. *Adv. Funct. Mater.* **2025**, *35*, 2417215.

[52] Ma, Z. H.; Yang, K.; Li, D.; Liu, H.; Hui, S. C.; Jiang, Y. Y.; Li, S. Y.; Li, Y. M.; Yang, W.; Wu, H. J. et al. The electron migration polarization boosting electromagnetic wave absorption based on Ce atoms modulated yolk@shell Fe_xN@NGC. *Adv. Mater.* **2024**, *36*, 2314233.

[53] Yadav, P.; Choudhary, R. J.; Phase, D. M.; Raghunathan, R. Study of structural and magnetic properties of Gd_2MoO_6 compound. In *AIP Conference Proceedings*, Kerala, India, 2019, 020031.

[54] Huang, W. Q.; Yang, Y. H.; Gu, H. Y.; Yu, W. J.; Shao, G. F. A core–shell carbon-ceramic fibrous aerogel derived from aramid-polysilsesquioxane for broadband electromagnetic wave absorption. *J. Mater. Chem. C* **2025**, *13*, 10658–10670.

[55] Yu, W. J.; Shao, G. F. Morphology engineering of defective graphene for microwave absorption. *J. Colloid Interface Sci.* **2023**, *640*, 680–687.

This is an open access article under the terms of the Creative Commons Attribution 4.0 International License (CC BY 4.0, https://creativecommons.org/licenses/by/4.0/).

© The Author(s) 2027. Published by Tsinghua University Press.